

A.1 Overview of data from literature used in Figure 1 of main text

Type	Description	Pressure (kbar)*	notes	T (°C) (other)	notes	a_{TiO_2}	notes	T (°C) (TH10)	T (°C) (HA12)
Volcanic	Bandelier	1.5-2.5		815-883		0.13-0.26		622-727	781-909
	Taupo	1.0-2.0	Independent pressure estimates based on melt inclusion studies, phase equilibria constraints, and seismic evidence (cf. Kularatne and Audetat, 2014, and references therein)	726-771	Zircon saturation temperatures based on melt inclusion compositions along the same growth zones as entrapped zircons	0.6-0.85	Based on melt inclusion compositions and TiO_2 solubility model of Kularatne and Audetat (2014), which agrees with Hayden and Watson (2007)	564-657	678-811
	Toba	1.0-3.0		726-741		0.20-0.32		529-609	649-778
	Fish Canyon	1.9-2.9		724-727		0.88-1.05		564-601	713-766
	Bishop Tuff	2.2-3.2		727-731		0.52-0.54		553-584	687-719
Plutonic	Tuolumne Granodiorite	1.6-2.4 (2.0)	Al-in-hbl ¹	>650	Accepted solidus	0.5-0.6	Presence of titanite	488-544 ¹	617-688 ¹
	Butte Granite	2-2.5	Al-in hbl ⁴	740-760	X_{Mg} -Ti-in-bio thermometry ⁵	0.5	Subsolidus exsolution of rutile in qtz	596-669 ⁵	760-842 ⁵
	Porphyry dikes in Butte Granite	0.7-2.5	hydrostatic to lithostatic ⁵	-	only Ti in qtz	0.5	Subsolidus exsolution of rutile in qtz	562-578 ⁵	716-747 ⁵
Magmatic-Hydrothermal Transition	Early dark mica (EDM) veins and biotite crackles	1.7-2.7 (2.5)	fluid inclusions ⁹	459-659 550-700 520-700 550-700	Zr-in-rutile ⁵ Na-K partitioning between kfs and msc ² X Mg-Ti-in-bio thermometry ⁵ Fe-Ti oxides ⁷	1	Presence of rutile	401-467 ⁵	512-594 ⁵
	Barren Quartz/Quartz-molybdenite veins	1.7-2.7 (2.5)	fluid inclusions ⁹	550-650 550-650 508-634	S isotope thermometry on adjacent molybdenite-anhydrite grains ³ fluid inclusions ⁹ Zr-in-rutile ⁵	1	Presence of rutile	443-543 ⁵	564-697 ⁵
	Pyrite-quartz veins (GS = gray sericite)	0.4-0.7	fluid inclusions and Zr-in-rutile ⁹	370-450 498 (n=1) 450-550	fluid inclusions ⁹ Zr-in-rutile ⁵ Thermodynamic modeling ⁶	1 1	Presence of rutile	381-425 ⁵	458-510 ⁵
	Main stage veins	0.2-0.6 (0.4)	Hydrostatic, fluid inclusions ⁹	230-400	Fluid inclusions ⁹	1	Presence of rutile	<373 ⁵	<431 ⁵

* Bold indicates value used in calculation

1. Ackerson M.R., Mysen B.O., Tailby N.D. and Watson E.B., Low-temperature crystallization of granites and the implications for crustal magmatism, *Nature* **559**, 2018, 94–97.
2. Brimhall G.H., Early Fracture-Controlled Disseminated Mineralization at Butte, Montana. *Econ. Geol.* **72**, 1977, 37–59.
3. Field C.W., Zhang L., Dilles J.H., Rye R.O. and Reed M.H., Sulfur and oxygen isotopic record in sulfate and sulfide minerals of early, deep, pre-Main Stage porphyry Cu-Mo and late Main Stage base-metal mineral deposits, Butte district Montana, *Chem. Geol.* **215**, 2005, 61–93.
4. Houston R.A. and Dilles J.H., Structural geologic evolution of the Butte district, Montana, *Econ. Geol.* **108**, 2013, 1397–1424.
5. Mercer C.N. and Reed M.H., Porphyry Cu-Mo stockwork formation by dynamic, transient hydrothermal pulses: Mineralogic insights from the deposit at Butte, Montana, *Econ. Geol.* **108**, 2013, 1347–1377.
6. Reed M., Rusk B. and Palandri J., The Butte magmatic-hydrothermal system: One fluid yields all alteration and veins, *Econ. Geol.* **108**, 2013, 1379–1396.
7. Roberts S.A., Early hydrothermal alteration and mineralization in the Butte district, Montana: Ph.D. dissertation, 1975, Harvard University, 157 p.
8. Rusk B.G., Reed M.H., Dilles J.H. and Kent A.J.R., Intensity of quartz cathodoluminescence and trace-element content in quartz from the porphyry copper deposit at Butte, Montana, *Am. Mineral.* **91**, 2006, 1300–1312.
9. Rusk B.G., Reed M.H. and Dilles J.H., Fluid inclusion Evidence for Magmatic-hydrothermal Fluid Evolution in the Porphyry Copper-Molybdenum Deposit at Butte, Montana, *Econ. Geol.* **103**, 2008, 307–334.

A.2 PFIB extraction for EPMA analysis

To empirically quantify the amount of secondary fluorescence in our data set, and to assess the accuracy of the PENEPMa modeling, we devised a novel sample preparation method that allowed us to isolate outer quartz crystals from Qz29_ana and analyze them on the microprobe with no SF at all.

After an initial EPMA analysis, we put the polished mount into the Helios G4 PFIB (plasma focused ion beam) UXe DualBeam scanning electron microscope. This machine is unique from other FIB-SEMs in that it can use Xe as an ion source. Beam current was set to 0.5 μ A. We milled a 70 μ m deep moat around two rectangular areas 40 μ m x 30 μ m in dimension. For one region, we then milled away any Ti particles within 200 microns of the target (Fig. A1a). For the second region, after we had milled the vertical moat we tilted the sample and began to create a wedge shape. Once a wedge geometry had been established, we tilted the sample 72° from the ion beam and line-cut to bisect the wedge ~8.5 μ m below the surface. We milled most of the way through the wedge, then attached the omniprobe micromanipulator to one edge of the rectangular area with carbon at 12 kV. After the omniprobe was adhered to the region, we finished milling all the way through the bottom of the wedge and removed the region from the rest of the sample (Fig. A1d). The ion hewn surface was relatively flat (Fig. A1c).

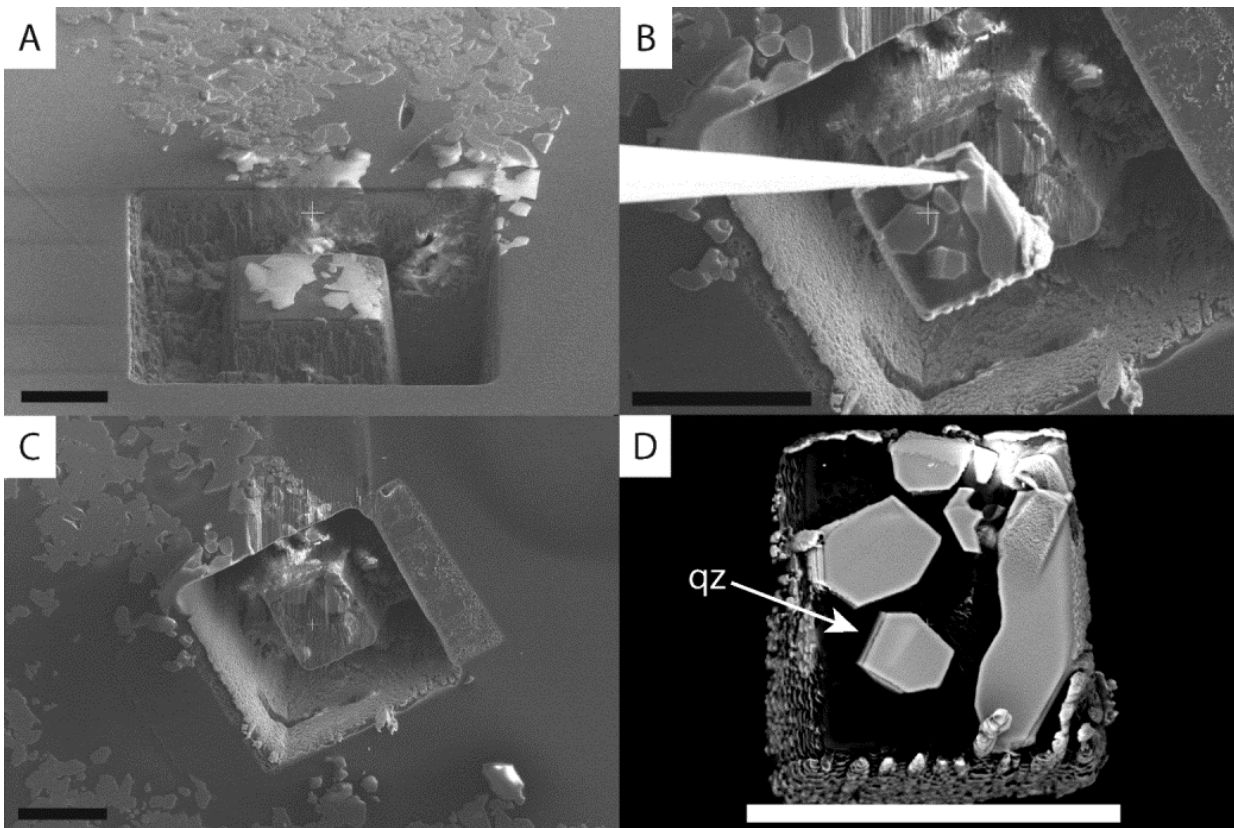


Figure A1. The steps taken on the PFIB to prepare the sample for microprobe analysis sans secondary fluorescence. A) the moat dug around the crystals of interest B) the region of interest being removed from the mount with the omniprobe. C) the region that was cut using the ion milling process, showing how flat it is. D) the region of interest after being adhered to a carbon tab.

Having successfully removed a small region of interest from the larger sample, we retracted the omniprobe, vented the chamber, and inserted a carbon tab adhered to an SEM mount. When the chamber was at pressure and the beams were back on, we inserted the omniprobe along with the region that had been lifted out and adhered it to the carbon tab. We then milled away the tip of the needle that was attached to the sample, leaving behind the flat, polished region (Fig. A1d). Next, we analyzed the two regions prepared on the PFIB-SEM on the microprobe using the procedures outlined in the main text. Two crystals were analyzed and came back at 508 ppm Ti and 594 ppm Ti.

It is important to note that this technique precluded the analysis of many crystals and is quite time intensive. The method is limited to preparing only a few grains at once because often, after one has moated out a region of interest (or even having gone so far as to remove a region of interest), it will become evident that there are TiO_2 crystals immediately beneath what was a seemingly TiO_2 free zone. Due to the small size of the crystals, it is rarely possible to mill away the TiO_2 crystals while preserving enough material to analyze with the microprobe.

A.3 PENEPEMA modeling of secondary fluorescence

Secondary fluorescence (SF) is the phenomenon whereby primary characteristic and bremsstrahlung (continuum) x-rays generated in the interaction volume (the region of the sample in which the incident electron beam comes to rest within) penetrate any surrounding phases. That is, if another phase is present in the sample, near to the beam incident location, and that surrounding phase contains non-trace amounts of the element of interest, x-rays of interest will be generated within the adjacent phase. This will result in erroneously high concentrations measured for these trace elements.

Ti ka, in SiO_2 adjacent to TiO_2 (15 keV, TiO_2 std)

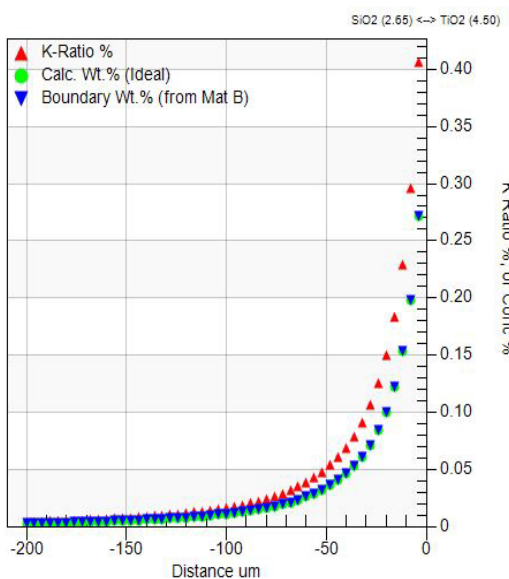


Figure A2. The magnitude of the erroneously high Ti concentration measured in quartz as a function of distance from an infinitely long planar boundary of TiO_2 (the Concentration % units are wt%). The effect is no longer seen by the time the beam is ~150 microns away from the boundary. This is the absolute worst-case scenario for SF contamination of Ti in quartz.

Thus, SF is a serious problem for measuring Ti in quartz when one imposes the criterion for thermodynamic equilibrium that a pure rutile phase co-precipitated with the quartz of interest, as this usually entails finding a rutile crystal close to or as an inclusion in the quartz being measured. In the worst case scenario where one is measuring Ti in quartz near an infinite planar boundary of pure TiO_2 , the beam must be ~150 μm away from the boundary to minimize any SF effects, as modeled by the Penfluor GUI in CalcZAF/Standard (Fig. A2). Fortunately, the electron microprobe is a “mature” technique and, the magnitude of the SF effect has been quantified by modeling and confirmed for many materials by measurements performed near synthetic boundaries in several geometries. Beyond measuring the SF effect, which is tedious and time-consuming, it has been shown that Monte Carlo simulations can accurately and precisely predict the magnitude of these SF effects on trace element measurements even for non-planar geometries. Therefore, one can first model for possible SF effects, and recognize whether SF is a problem at the expected level of EPMA sensitivity, next one can then measure the trace element of interest, model the geometry of the phases present in the sample, and subtract the modeled SF value from the measured value to get the true concentration (for example, using the program CalcZAF/Standard which provides a GUI for the Penepma 2012 Monte Carlo modeling software).

To perform corrections for SF effects of TiO_2 grains near to quartz grains, we used PENEPMa (Llovet and Salvat, 2017) to model how secondary x-rays generated in a 5 μm TiO_2 phase are transmitted through epoxy and silica. We chose 5 μm because it was the maximum size of the TiO_2 particles in our outer capsule run products, and epoxy and silica were chosen as transmitting mediums because the crystals we measured were small (10-20 μm) quartz crystals separated from each other and the TiO_2 phase by epoxy. All measurements were taken \sim 40 microns or more away from any TiO_2 particles. The geometry used for the PENEPMa runs was that of a 5 μm TiO_2 sphere separated from a 20 μm SiO_2 sphere by 40 μm of epoxy where the electron beam was centered on the 20 μm quartz grain. The results of the Penepma modeling are presented in Table A2. For analyses where multiple particles of TiO_2 are present, the total amount of SF in the acquired data set can be estimated by multiplying the modeled value for a single particle by the number of particles at the same distance from the beam incident location.

Distance of beam from inclusion	S.F. effect	matrix
10.00	19 ± 2 ppm Ti	SiO_2
20.00	10 ± 1 ppm Ti	SiO_2
40.00	3 ± 1 ppm Ti	SiO_2
10.00	21 ± 2 ppm Ti	epoxy
20.00	11 ± 1 ppm Ti	epoxy
40.00	5 ± 1 ppm Ti	epoxy

Table A2. Model results of the magnitude of secondary fluorescence caused by a 5 micron particle of TiO_2 surrounded in either quartz or epoxy.

For details on how to do these calculations, please see <https://probesoftware.com/smf/index.php?topic=58.0>.

Reference

Llovet, Xavier, and Francesc Salvat. "PENEPMa: A Monte Carlo program for the simulation of X-ray emission in electron probe microanalysis." *Microscopy and Microanalysis* 23.3 (2017): 634-646.

A.4 Identification of Polymorphs

Polymorphs of crystalline titania and silica were variably identified with Raman spectroscopy and transmission electron microscope- single area electron diffraction patterns (TEM-SAED). Raman was used because it is fast, but the method is unsuited for differentiating between different crystal morphologies because the data is acquired on polished samples. TEM, in contrast, requires laborious and time-consuming sample prep but allows for each crystal morphology to be separately identified. Below are representative examples of Raman spectra of tridymite, rutile, and anatase (Fig. A3), TEM- SAED patterns used to identify phases of (Fig. A4), and rutile inclusion in quartz overgrowth and it's SAED pattern (Fig. A5).

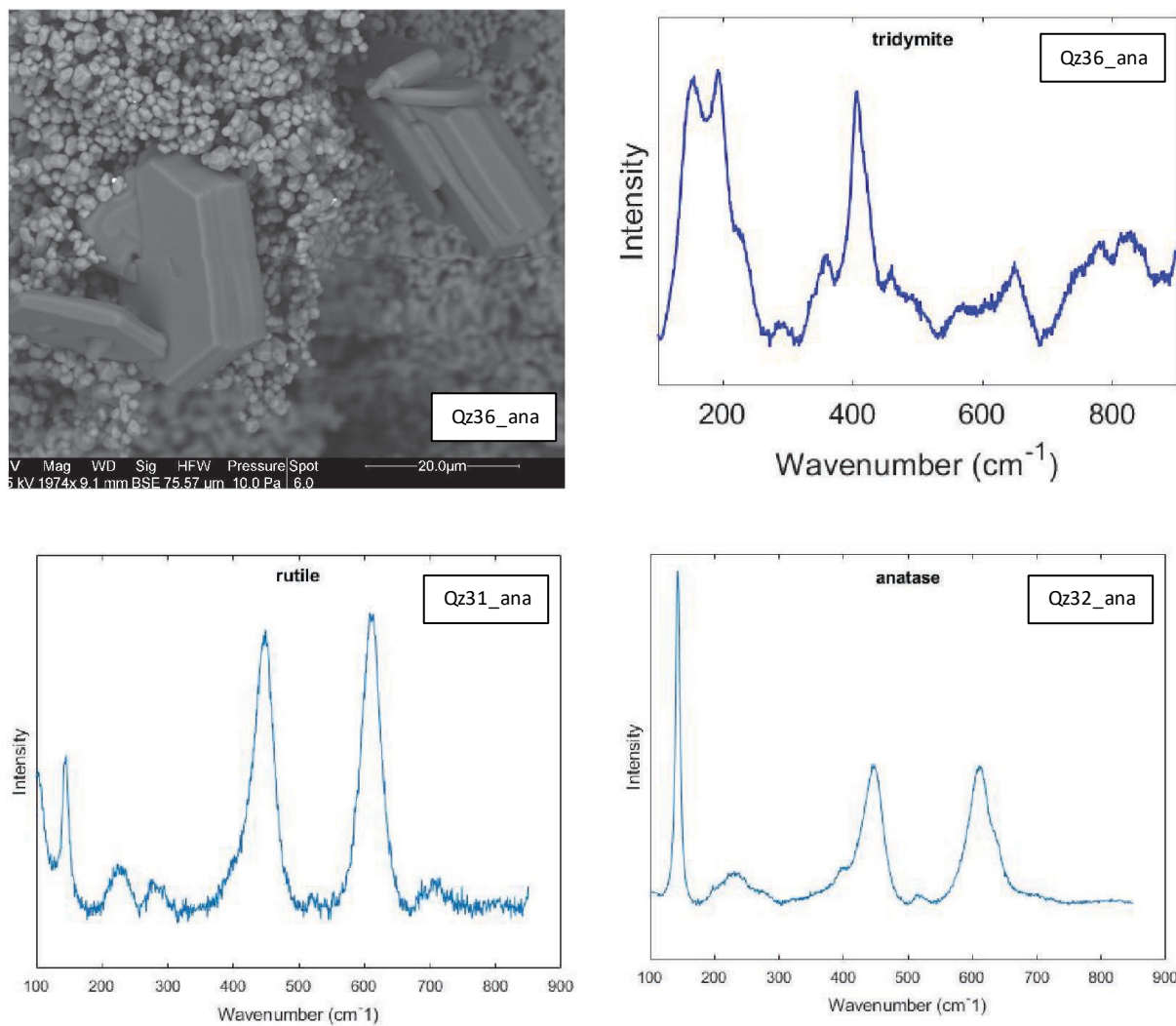


Figure A3. Hexagonal platelets and columns (SEM-BSE image in upper right panel) were imaged in many experiments and some were identified via Raman spectroscopy. Spectra of relevant phases were identified by comparison against reference spectra in the Rruff mineral database online.

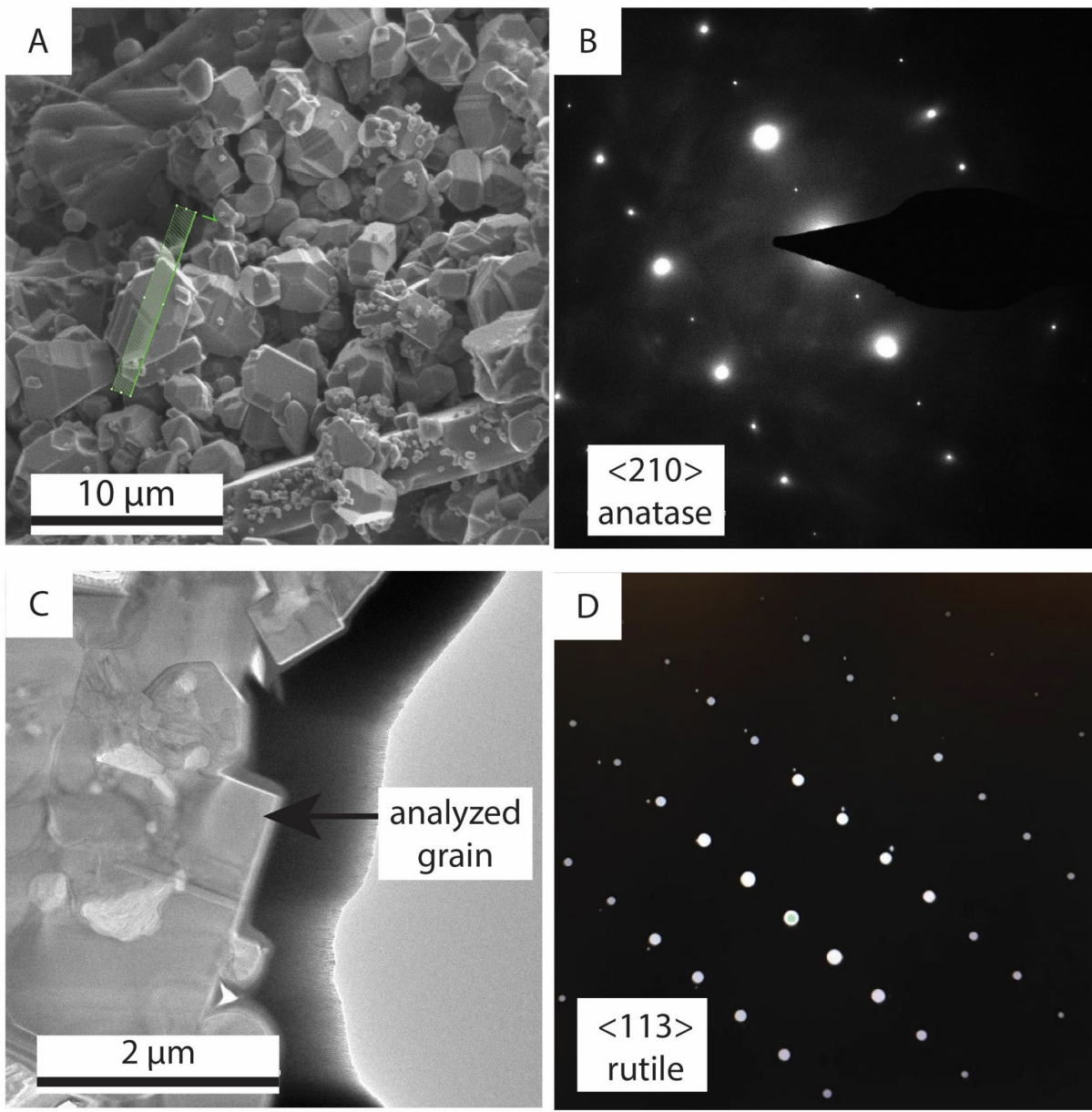


Figure A4. Anatase and rutile crystals identified with TEM-SAED from Qz32_ana. A) Loose crystals of TiO_2 displaying a variety of habits. The green rectangular region bisects the crystal that was made into the TEM sample that yielded B) the $\langle 210 \rangle$ zone of anatase collected from the crystal shown in panel A. C) A TEM brightfield image of a rectangular TiO_2 grain that yielded D) the SAED pattern of the $\langle 113 \rangle$ zone of rutile.

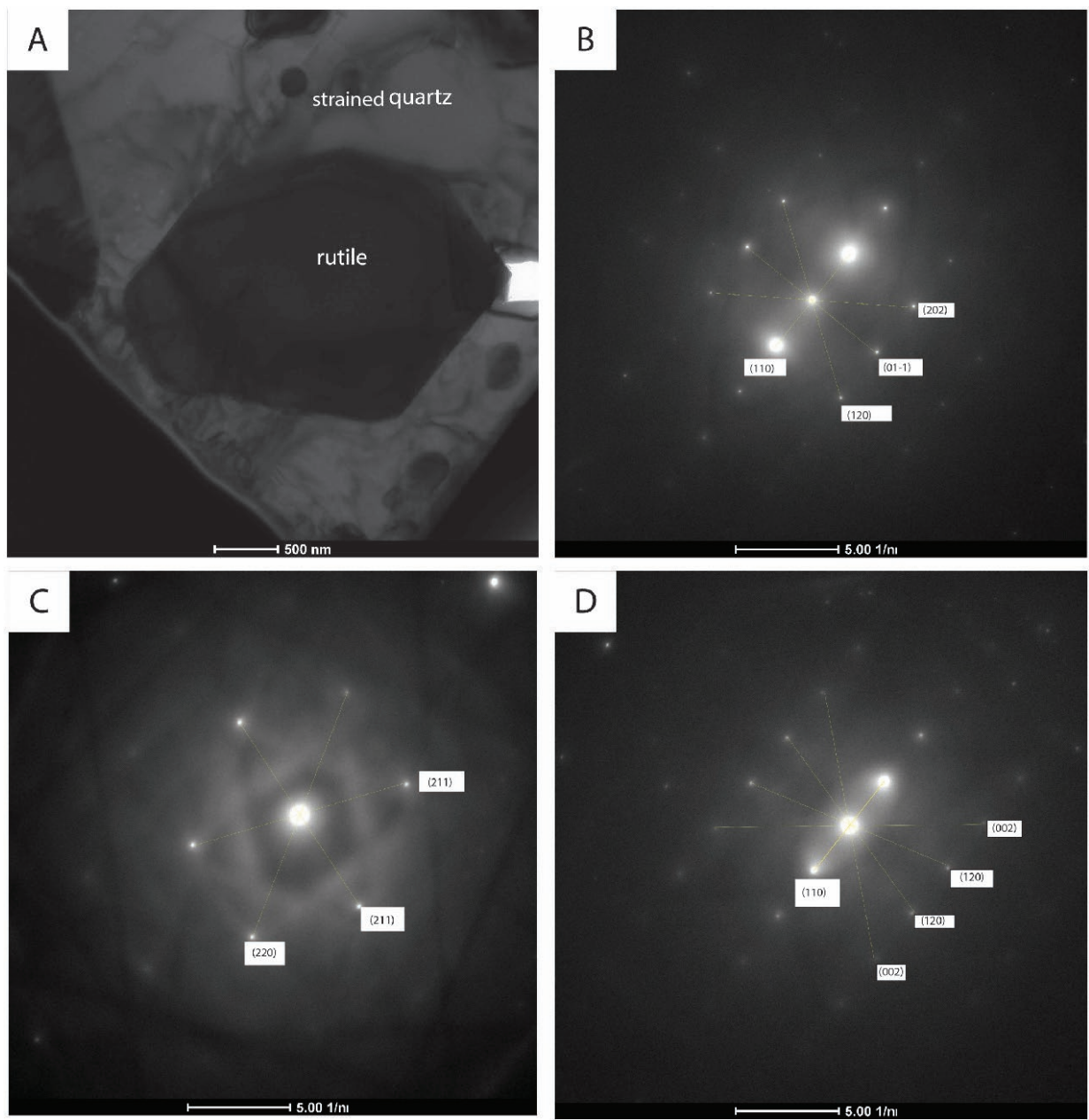


Figure A5. Rutile inclusions surrounded by strained quartz overgrowth from Qz19_ana, an experiment done with a 50:50 mix by weight of SiO_2 to TiO_2 that yielded an overgrowth with abundant TiO_2 inclusions. A) a CCD (charge coupled device) image taken with the TEM showing the euhedral rutile inclusion surrounded by a strained quartz lattice. B-D) SAED reflectors annotated with the Miller indices of the crystal planes that made them.

A.5 SEM-CL and SE Images of Analyzed Overgrowths

